



Cite this: DOI: 10.1039/d3tc01774e

Efficient generation of highly crystalline carbon quantum dots *via* electrooxidation of ethanol for rapid photodegradation of organic dyes†

Santiago D. Barrionuevo,^{ib} ^a Federico Fioravanti,^b Jorge M. Nuñez,^{cdefg} Mauricio Llaver,^h Myriam H. Aguirre,^{ib} ^{fgi} Martín G. Bellino,^{ib} ^j Gabriela I. Lacconi,^b and Francisco J. Ibañez ^{ib} ^{*a}

Achieving versatile routes to generate crystalline carbon-based nanostructures has become a fervent pursuit in photocatalysis-related fields. We demonstrate that the direct electrooxidation of ethanol, performed on Ni foam, yields ultra-small and highly crystalline graphene-like structures named carbon quantum dots (CQDs). We perform simulations of various sp^2 and sp^3 domains in order to understand the optical properties of CQDs by accounting their contribution as absorbance/luminescent centers in the overall optical response. Experiments and simulations reveal that absorbance bands for as-synthesized CQDs are dominated by small sp^2 domains comprised of ≤ 7 aromatic-rings. After 48 h synthesis, the dispersion transition from yellow to red, exhibiting new and red shifted absorbance bands. Furthermore, fluorescence emission is governed by medium-sized sp^2 domains (with aromatic ring counts ≤ 12) and oxygen-containing groups. These oxygen-rich groups within the CQDs, confirmed by FT-IR and XPS, are responsible for the fast photodegradation of organic dyes, with $\sim 90\%$ of methylene blue (MB) being degraded within the first 5 min of light exposure. Our work provides crucial insights about the electrochemical synthesis and overall optical properties of carbon nanostructures, while being effective and reliable toward the degradation of contaminants in water.

Received 23rd May 2023,
Accepted 29th July 2023

DOI: 10.1039/d3tc01774e

rsc.li/materials-c

Introduction

Carbon-based nanoparticles (CNPs) are pivotal in multiple applications due to outstanding optoelectronic properties derived from quantum confinement, functional groups, and the type of synthesis performed. As a result, they have become essential in a wide range of applications. CNPs are used as fluorescent probes for medical diagnosis,¹ selective detection of water contaminants,^{2,3} as effective photosensitizers in the design of photoanodes,⁴ and as efficient photocatalyst for water splitting⁵ and photodegradation of contaminants in water⁶ among other applications. There is a large number of bottom-up and top-down methods to obtain CNPs that, involves low-molecular-weight molecules in the case of the former and large carbon precursors for the latter.⁷ Bottom-up methods include solvothermal, electrochemical, pyrolysis, and microwave-assisted synthesis, among others.⁸ Electrochemical-based methods are often preferred due to their low cost, high yield, and ability to provide precise control over reaction parameters, leading to improved selectivity. The proposed mechanism involves electrooxidation, cross-linking, and finally dehydration steps which enables CNPs with high oxygen content.⁹ These low-molecular weight precursors involved in

^a Instituto de Investigaciones Físicoquímicas, Teóricas y Aplicadas (INIFTA), Universidad Nacional de La Plata – CONICET, Sucursal 4 Casilla de Correo 16, 1900 La Plata, Argentina. E-mail: fjiban@inifta.unlp.edu.ar

^b INFIQC-CONICET, Dpto. de Físicoquímica, Facultad de Ciencias Químicas, Universidad Nacional de Córdoba, Ciudad Universitaria, 5000 Córdoba, Argentina

^c Resonancias Magnéticas-Centro Atómico Bariloche (CNEA, CONICET), S. C. Bariloche, 8400, Río Negro, Argentina

^d Instituto de Nanociencia y Nanotecnología, CNEA, CONICET, S. C. Bariloche 8400, Río Negro, Argentina

^e Instituto Balseiro (UNCuyo, CNEA), Av. Bustillo 9500, S.C. de Bariloche, 8400, Río Negro, Argentina

^f Instituto de Nanociencia y Materiales de Aragón, CSIC-Universidad de Zaragoza, C/Pedro Cerbuna 12, 50009, Zaragoza, Spain

^g Laboratorio de Microscopías Avanzadas, Universidad de Zaragoza, Mariano Esquillor s/n, 50018, Zaragoza, Spain

^h Laboratorio de Química Analítica para Investigación y Desarrollo (QUIANID), Facultad de Ciencias Exactas y Naturales, Universidad Nacional de Cuyo/Instituto Interdisciplinario de Ciencias Básicas (ICB), CONICET UNCUIYO, Padre J. Contreras 1300, 5500 Mendoza, Argentina

ⁱ Dpto. de Física de la Materia Condensada, Universidad de Zaragoza, C/Pedro Cerbuna 12, 50009, Zaragoza, Spain

^j Instituto de Nanociencia y Nanotecnología CNEA-CONICET, Av. Gral. Paz, 1499, San Martín, Buenos Aires, B1650, Argentina

† Electronic supplementary information (ESI) available. See DOI: <https://doi.org/10.1039/d3tc01774e>

the electrochemistry may include, for example, alcohols,¹⁰ citrate,¹¹ ionic liquids,¹² organic amines,¹³ and chiral molecules.¹⁴ Deng *et al.* first performed electrochemical synthesis directly from ethanol and demonstrated control over the size but not their structure, producing a high yield of amorphous CNPs.¹⁰ Crystalline nature of CQDs significantly alters their physical properties, particularly their optical characteristics. As a result, obtaining crystalline carbon quantum dots (CQDs) through direct electrooxidation of ethanol poses a major opportunity.

Optical properties in CNPs are not as straight forward as in semiconducting quantum dots where the band gap has a direct correlation with size.¹⁵ In fact, they need to be explained by multiple interplaying factors that mainly involve size,¹⁶ edge geometry (armchair or zig-zag),¹⁷ sp²/sp³ hybridization ratio,¹⁸ number of layers (thickness), and functional groups¹⁹ present within the surface/edge of the carbogenic cores. Kim *et al.* studied the effect of size and shape on the optical properties of carbon nanostructures.²⁰ They demonstrated that the absorption wavelength increased (red-shifted) as the size of CNPs increased and observed that circular shapes are comprised of an equal mixture of zig-zag and armchair borders. Recent studies suggest that the optical properties of sp² carbon networks can be attributed to the collective contribution of various sp² polycyclic aromatic hydrocarbons (PAHs) present within the structure.²¹ These PAHs act as individual absorption/luminescent centers.^{21–24} For instance, Urban and co-workers combined three different types of PAHs embedded in a polymer matrix in order to compare their optical properties with CNPs obtained experimentally.²⁵ In another work, the high crystallinity of PAHs-built CNPs demonstrated outstanding optical properties such as strong absorption bands extending to the visible region and large molar extinction coefficients.²⁶ Computational tools have been also utilized to describe the optical properties of PAHs that may change with their specific structure or chemistry.^{23,27–29} For instance, Peng Chen and co-workers studied how the emission properties of alike-GQDs change with size, edge configuration, functional groups, and addition of heteroatoms.²⁸ Also, Zhang and co-workers employed time-dependent DFT (TD-DFT) to chemisorb five different types of oxygen-containing groups to the basal plane of graphene dots. They demonstrated that the incorporation and the position of these groups within the nanostructure greatly altered the optical selection rules causing much broader absorption and emission bands as compared to sp² pristine carbon.²⁷ Another example is Melia *et al.* who simulated linear- and hexagonal-shaped PAHs and demonstrated distinct absorption bands based on the number of benzene units and aspect ratio.²³ Despite the significant progress made in the field, characterizing the optical properties of carbon-based nanostructures, by considering the complex interplay between their constituents, remains uncertain.

In this work, we report an electrochemical synthesis of crystalline and ultra-small size CQDs obtained *via* direct electrooxidation of ethanol to ultimately test them upon photocatalytic degradation of organic dyes. The synthesized product

comprises a population of crystalline carbon nanostructures with ≤ 3.0 nm diameter and 2–3 graphene layers thickness. We investigated the optical properties of the synthesized CQDs by designing and simulating sp² and sp³ subdomains that are assumed to coexist within the basal plane and the border of these carbon nanostructures. It should be mentioned that simulated oxygen-containing groups were only added at the borders of the PAHs subdomains to prevent the disruption of the sp² structure. Therefore, different types of sp² PAHs were simulated in order to search for potential matches with optical bands obtained experimentally. We were able to assign and classify various sp² subdomains along with oxygen-containing groups potentially present for as-synthesized and 48 h post-synthesis. The presence of hydroxyl- and carbonyl-terminated CQDs are most likely responsible for the photodegradation of methylene blue (MB) *via* the formation of radical species upon 250–750 nm irradiation lamps. Synthesized CQDs demonstrates outstanding kinetics of photodegradation by removing $\sim 90\%$ of the dye within the first 5 min of irradiation. This work has direct implications for achieving simple and scalable electrochemical synthesis of crystalline nanostructures as well as for further understanding of the optical characteristics of these carbon nanostructures toward optoelectronic applications.

Experimental methods

Reagents

All chemical reagents were used as received. Ethanol (99%), Sodium Hydroxide, Methylene Blue were purchased in Sigma-Aldrich Argentina. Aqueous solutions were prepared with ultrapure water (18.2 m Ω resistivity). Ni foam with thickness = 1.6 mm and porosity = 87% was purchased from MTI Corp. (Richmond, CA, USA). H₂ (99.999%) and CH₄ (99.999%) were purchased locally from Linde, Argentina.

Carbon quantum dots (CQDs) synthesis

CQDs were obtained through an electrochemical synthesis formed by Ni foam (anode) and Cu electrodes immersed in 0.1 M NaOH previously dissolved in Ethanol (99% v/v) electrolyte and subjected to 30 V during 60 min. As-synthesized dispersions exhibited basic pH ~ 11.0 . For purification of the product, the dispersion was centrifuged at 10 000 rpm in ethanol, filtered with hydrophilic micro-disks, dried off, and redispersed in nanopure water before use. A detailed study regarding ethanol electrooxidation in alkaline media (using Ni foams) along with some insights of CQDs formation mechanisms are included in S.1 and S.2 (ESI[†]); respectively.

Characterization

Structural. Imaging of nanostructures and structural characterization were performed by High-Resolution Transmission Microscopy (HR-TEM) using an aberration (Objective Lens) corrected Titan³ 60–300 (ThermoFisher) microscope operating at 80 kV at room temperature. Atomic Force Microscopy (AFM)

images were obtained using a Nanoscope V (Veeco) microscope in tapping mode. Samples were diluted in absolute ethanol (1:10000) and drop-cast deposited on mica for AFM analysis.

Spectroscopy. UV-vis absorbance spectra were recorded using a PerkinElmer LAMBDA 1050+ UV/Vis/NIR Spectrophotometer. Fluorescence emission and excitation spectra were acquired using a Horiba Fluorolog3 and a standard quartz cuvette. UV-vis and fluorescence samples were diluted in a 1/100 dilution using absolute ethanol. Attenuated Total Reflectance-Fourier Transform-Infrared (ATR-FT-IR) spectra were obtained using a PerkinElmer (Beaconsfield, UK) Spectrum Two instrument with a Universal ATR module. XPS data were collected using a Thermo Fisher Scientific Model K-alpha + with Al K α radiation at 1486.69 eV (150 W, 10 mA), charge neutralizer and a delay line detector (DLD) consisting of three multi-channel plates. Survey spectra were recorded from -5.0 to 1350 eV at a pass energy of 150 eV (number of sweeps: 2) using an energy step size of 1.0 eV and a dwell time of 100 ms. High resolution spectra for C 1s and O 1s were recorded in the appropriate regions, using an energy step size of 0.1 eV.

Electrochemical. Cyclic voltammograms (CVs) were run in a CHI 700D electrochemical station employing a Ni foam and Pt as working and counter electrodes; respectively. The reference voltage is set through an Ag/AgCl reference electrode submerged in an electrolytic solution of 1.0 M NaOH for the control group and 1.0 M NaOH + 0.5 M ethanol for the test group. For the electrooxidation of ethanol, all the cyclic voltammograms were recorded 10 times in the range of 0–1.6 V.

Computational. Calculations were carried out using ORCA quantum Chemistry Package.³⁰ Ground state geometries of current simulated systems were firstly optimized with DFT using the BP86 functional with a SVP basis set and RIJCOSX approximation using a DEF/JAUX basis set. All dangling bonds were passivated with H atoms. Absorption UV-vis spectra as well as emission spectra were calculated using a TD-DFT method with B3LYP hybrid functional a DEF/J aux basis set without RIJCOSX approximation. Absorbance and fluorescence spectra are calculated using the ASA (Advanced Spectral Analysis) module in ORCA for each PAH.³¹

Photodegradation of methylene blue

A quartz cuvette containing solutions with different concentrations of MB (4.7×10^{-6} , 1.0×10^{-5} , and 3.0×10^{-5} M) and CQDs (0.2, 0.5, and 0.8 mg mL⁻¹) were mixed and exposed to UV-vis irradiation. Samples were irradiated with a 100 W Hg discharge lamp (Olympus LH100G) with a wavelength range between 250 to 750 nm. Aqueous solutions of MB and CQDs were stirred during 10 min in the dark previous to the photochemical process, in order to ensure the interaction between dye and the CQDs. The pH of MB was adjusted to 10.5 to match up with the pH of CQDs so greater stability and efficiency can be achieved. Monitoring of MB degradation was followed by UV-vis spectroscopy.

Results and discussion

Structural characterization of CQDs

Fig. 1(A) shows a 125×125 nm HR-TEM image for CQDs, along with a histogram indicating monodispersed and ~ 2.8 nm average diameter carbon dots with monomodal narrow Gaussian distribution corresponding to 0.75 nm full-width half-maximum (FWHM) shown below. Fig. 1(B) shows a selected CQD enclosed by a red square which is enlarged in Fig. 1(C) to clearly show its hexagonal symmetry and 0.21 nm lattice fringe corresponding to the reflection of planes of graphene. The observed crystallinity is assessed applying the Fast Fourier Transform (FFT) to the selected CQD as shown in Fig. 1(E). The FFT clearly exhibits a six-fold symmetry pattern and a reciprocal vector of 4.76 nm^{-1} (0.21 nm in real space) corresponding to $01\bar{1}0$, $10\bar{1}0$, $1\bar{1}00$, $0\bar{1}10$, $\bar{1}010$, $\bar{1}100$ reflections for graphene-like nanostructures. Fig. 1(F) shows inverse FFT obtained by applying a mask to the six diffraction points described before for the same spot. For comparison purposes, a simulated graphene structure is placed on top of the honeycomb lattice. Carbons in the alpha (α) and beta (β) positions of the hexagonal lattice are marked in red and blue; respectively. To further evaluate the crystalline structure of the CQDs, different areas of the sample were randomly examined. We observed, in some cases, that CQDs presented the same ~ 0.21 nm interlayer spacing but several different crystallographic orientations. Fig. S3 (ESI[†]) shows a close-up view for selected CQDs showing these features. Depending on the crystal orientation (respect to electron beam direction) some CQDs appeared as mere lattice fringes, this kind of structures only shows a simple FFT pattern composed of points in one direction, as seen in Fig. S4(A)–(C) (ESI[†]). Additionally, other evaluated areas of the sample exhibited features recently reported as nanodiamonds consistent with the work of Shen *et al.* who probed that bottom-up synthesis from alcohols could yield cubic carbon phases at low temperatures (423 K).³² Fig. S4E (ESI[†]) shows a possible candidate for this type of nanostructure. In general, the vast majority of the evaluated CQDs has shown monodisperse and highly crystalline structures, unlike amorphous carbon phases previously reported employing a similar electrosynthesis.¹⁰

Fig. 2(A) shows an AFM image of as-synthesized CQDs deposited on atomically flat mica along with a representative cross-section profile marked with a red line shown below. The cross-section indicates CQDs with thickness ranging from 2 to 4 graphene-like layers. Fig. 2(B) shows a histogram from several cross-sections measured from non-agglomerated CQDs depicted in Fig. 1(A). According to the AFM assessment, the sample comprises the majority of non-agglomerated CQDs exhibiting disk-like nanostructures as indicated by the 2–3 layers average height (~ 1.0 nm). It should be mentioned that higher height profiles of several nanometers were also found and attributed to stacked CQDs.

Experimental and simulated UV-vis absorbance bands for CQDs

As-synthesized CQDs exhibited crystalline structure and aspect ratio that are reminiscent of PAHs. To explain their optical

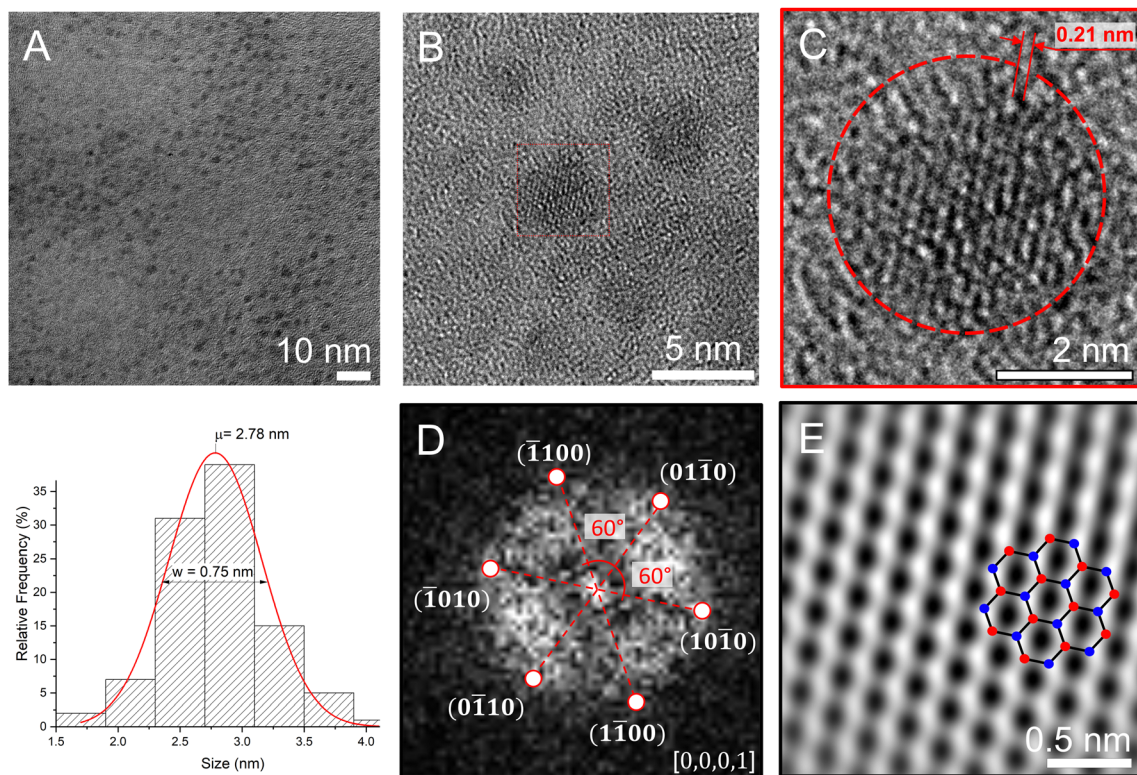


Fig. 1 Zoom-out HR-TEM images of carbon quantum dots (CQDs) (A) along with a histogram indicating ~ 2.8 nm average diameter shown below. Selected CQD enclosed by a red box (B) and its magnification showing 0.21 nm lattice fringe (C). Fast Fourier Transform of the selected CQD showing the corresponding six-fold symmetry (D) and inverse FFT (E), digital zoom with the predicted C atom positions.

properties, we designed and simulated the absorbance bands of several sp^2 and sp^3 subdomains in order to search for a match to the experimentally-obtained bands. Fig. 3(A) and (B) show simulated UV-vis absorbance bands of various PAHs, which fall within the experimental spectra measured for as-synthesized and 48 h post-synthesis; respectively. We chose these two stages based on the distinct color changes of the dispersion experienced over time (see Panel E). At the initial stage of synthesis, the solution looks transparent (Panel E) with no apparent absorbance bands (spectra not shown). As the synthesis continued to culmination at 60 min, the solution turned to a pale yellow (Panel E), and two bands appeared at ~ 275 nm and 330 nm as evidenced in Fig. 3(A). Deng *et al.* also obtained a prominent band close to 280 nm that became more intense with increasing voltage for amorphous carbon dots obtained under similar electrooxidation conditions.¹⁰ In addition, the yellow color and the band at ~ 275 nm have been previously observed, in the exact position, for CNPs electrochemically synthesized at room temperature using a graphite anode.³³ This band has been commonly ascribed to the $\pi-\pi^*$ transition of the aromatic sp^2 domains present within the structure and associated with the degree of oxidation³⁴ and quantum confinement^{20,35} of CNPs obtained from different types of syntheses. The main band at 275 nm is assigned to the contribution of coronene (hexagonal configuration of 7 aromatic rings) and naphthalene (2 linear rings). The description for all the simulated PAHs employed in this work is shown in Panel 3F. In addition, secondary bands

corresponding to benzo-e-pyrene (~ 330 nm) and benzo-ghi-perylene (~ 265 nm and ~ 374 nm) are also observed. The absorbance bands simulated here for coronene (~ 285 nm) falls within PAHs reported by our group²³ as well as UV-vis experiments performed by Patterson³⁶ and Fetzer.³⁷ Moreover, pyrene-like molecules observed experimentally at 335,³⁸ 345,²⁵ and 360 nm coincide with our simulations.²⁹ These bands also appeared in similar positions as described by Melia *et al.* who simulated various linear sp^2 (*i.e.*; anthracene) and hexagonal (*i.e.*; coronene) carbon nanostructures and determined that absorption bands do not extended beyond ~ 400 nm for ~ 7 aromatic rings despite their aspect ratio. Small shifts in UV-vis absorbance maximum values may also occur for different concentrations of the same PAH. It has been demonstrated that varying the concentration of a mixture of PAHs (anthracene/pyrene/perylene) perfectly resembles the bands obtained in the as-synthesized carbon nanoparticles.²⁵

At 48 h post-synthesis, the dispersion transitioned to red, the entire spectra became flattened and mounted, and the band at ~ 331 nm broaden and red shifted toward ~ 366 nm as seen in Panel E and Fig. 3(B). The band observed at ~ 366 nm can be ascribed to $n-\pi^*$ electronic transition corresponding to the incorporation of oxygen-containing groups (*i.e.*; carbonyl, epoxide, *etc.*). This is expected because these CQDs are continuously evolving over time into more complex carbon network of fully mixed sp^2 and sp^3 subdomains. The particular absorption band observed at 366 nm is attributed to circumbiphenyl PAH, which is circumscribed by hydroxyl groups as noted. There is another

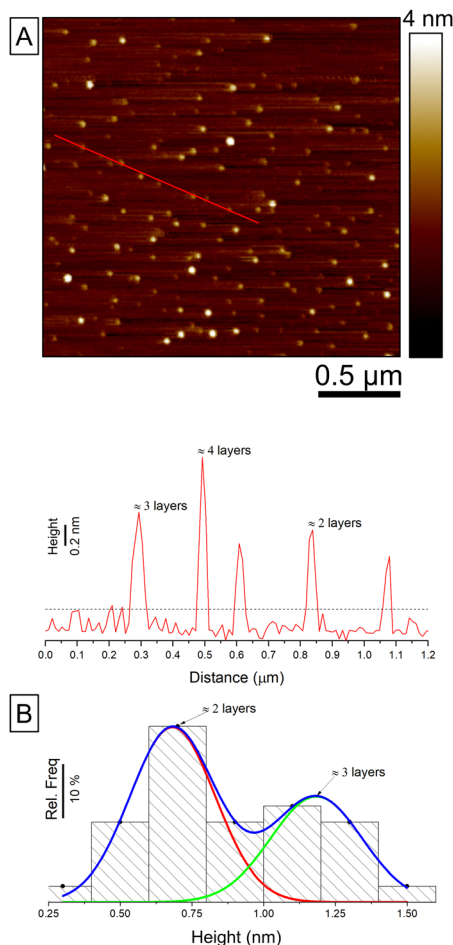


Fig. 2 AFM image (A) along with a representative cross-section profile for as-synthesized CQDs. Histogram of non-agglomerated carbon nanostructures observed in a $2 \times 2 \mu\text{m}$ drop-cast deposited on atomically flat mica (B). Average height indicates carbon structures comprised of 2–3 layers.

broad band that expands from 240 to 265 nm that was assigned to $\pi \rightarrow \pi^*$ transition of phenanthrene, chrysene, and pyrene sp^2 domains as indicated. It is important to note that those bands within the 240 to 255 nm range, as well as those at 366 nm are absent in the as-synthesized CQDs (Fig. 3(A)). Our simulations indicated that larger PAHs including ovalene, circumcoronene, circumbiphenyl, along with oxygen-containing groups located at the border are the ones responsible for red-shifting the absorbance band. For instance, pristine sp^2 pyrene has a prominent band at 336 nm that shifted to 380 nm upon the incorporation of two OH-functional groups at the border (Fig. S5, ESI[†]). In line with that, Fig. S6 (ESI[†]) exhibits simulated molecular orbitals of coronene-functionalized carbonyl group. The intermediate band between 325 to 340 nm is filled by $n \rightarrow \pi^*$ transitions of carbonyl groups modeled by a carbonyl-terminated naphthalene domains (1*H*,3*H*-benzo[*de*]isochromene-1,3-dione).

Experimental and simulated emission bands for CQDs

Fig. 3(C) and (D) exhibits the emission spectra of CQDs measured at 48 h post-synthesis at different excitation energies. The emission rate of CQDs depends on the excitation energy.

Our model predicts that different excitation energies will induce emissions from different isolated sp^2 subdomains within the carbogenic core. As observed for UV-vis absorbance hydroxyl- and carbonyl-terminated domains red shifted the emission bands. Fig. 3(C) depicts emission spectra for 230 nm excitation, being naphthalene (~ 282 nm) and circumbiphenyl (~ 340 nm) the dominant features of the spectra. Carbonyl-terminated naphthalene domains and hydroxyl-terminated circumbiphenyl emits in the region of 320 and 360 nm; respectively. Bands located between 340–400 nm emit due to quantum confinement of sp^2 subdomains within the carbogenic core.²⁸ Meanwhile, carbonyl- and hydroxyl-terminated sp^2 domains dominate over the extended emission into the visible range of the spectrum. For excitation wavelengths above 360 nm, the emission intensity decreases substantially and becomes dominated by the emission of oxygen-rich functional groups as well as medium size sp^2 PAHs subdomains including circumcoronene, circumbiphenyl, and ovalene. Fig. 3(E) and (F) exhibit optical pictures indicating the evolution of color during the electrochemical synthesis and a scheme of a simulated CQD fully comprised of sp^2 and sp^3 groups; respectively.

XPS and FT-IR spectroscopy

Fig. 4 compiles XPS and ATR-IR spectra measured for as-prepared CQDs. Fig. 4(A) and (B) exhibits deconvoluted C 1s and O 1s XPS spectra for 48 h CQDs; respectively. Fig. 4(A) indicates the presence of both, sp^2 and sp^3 peaks seen at 284.4 and 285.0 eV; respectively. It also exhibits two prominent peaks at higher binding energies (BE) observed at 286.8 and 289.0 eV assigned to sp^3 hybridization corresponding to epoxide and carbonyl groups; respectively. Fig. 3(B) shows deconvoluted O 1s XPS spectra for CQDs which is dominated by epoxide groups observed at 533.0 eV suggesting a strong oxidation of the surface/edge within the carbon structure. This is consistent with the simulated and experimental bands observed at 48 h after synthesis. A minor peak seen at ~ 536 eV is assigned to Na Auger corresponding to synthesis byproducts.³⁹ Assignment of peaks were referenced to Thermo Scientific Avantage Data System for XPS⁴⁰ and NIST X-ray Photoelectron Spectroscopy Database.⁴¹ Fig. 4(C) shows ATR-IR bands located at $\sim 880/780$, ~ 1050 , ~ 1110 , ~ 1425 – 1336 , ~ 1580 , ~ 1778 , ~ 2960 – 2850 , ~ 3300 (broad) and ~ 3662 (narrow) corresponding to C–H out of plane bend, C–O stretch of primary alcohols, C–O–C stretching arising from cyclic and alkyl-substituted ethers, C–H asymmetric/symmetric bending, C=C sp^2 aromatic ring stretching, C=O stretch, C–H asymmetric/symmetric stretching and bonded/non-bonded O–H hydroxyl groups, respectively. Analysis and peak assignment for ATR-IR were performed according to Coates *et al.*⁴² These results are consistent with XPS measurements due to several similarities. First, the C 1s XPS records C=C sp^2 and sp^3 bands, which are confirmed by FT-IR bands located at 1580 cm^{-1} (C=C sp^2) and in the region 1420 – 1050 cm^{-1} were several peaks corresponding to C–H/C–O groups with sp^3 hybridized carbon are observed. Furthermore, both XPS and ATR-IR confirms the presence of C–O groups

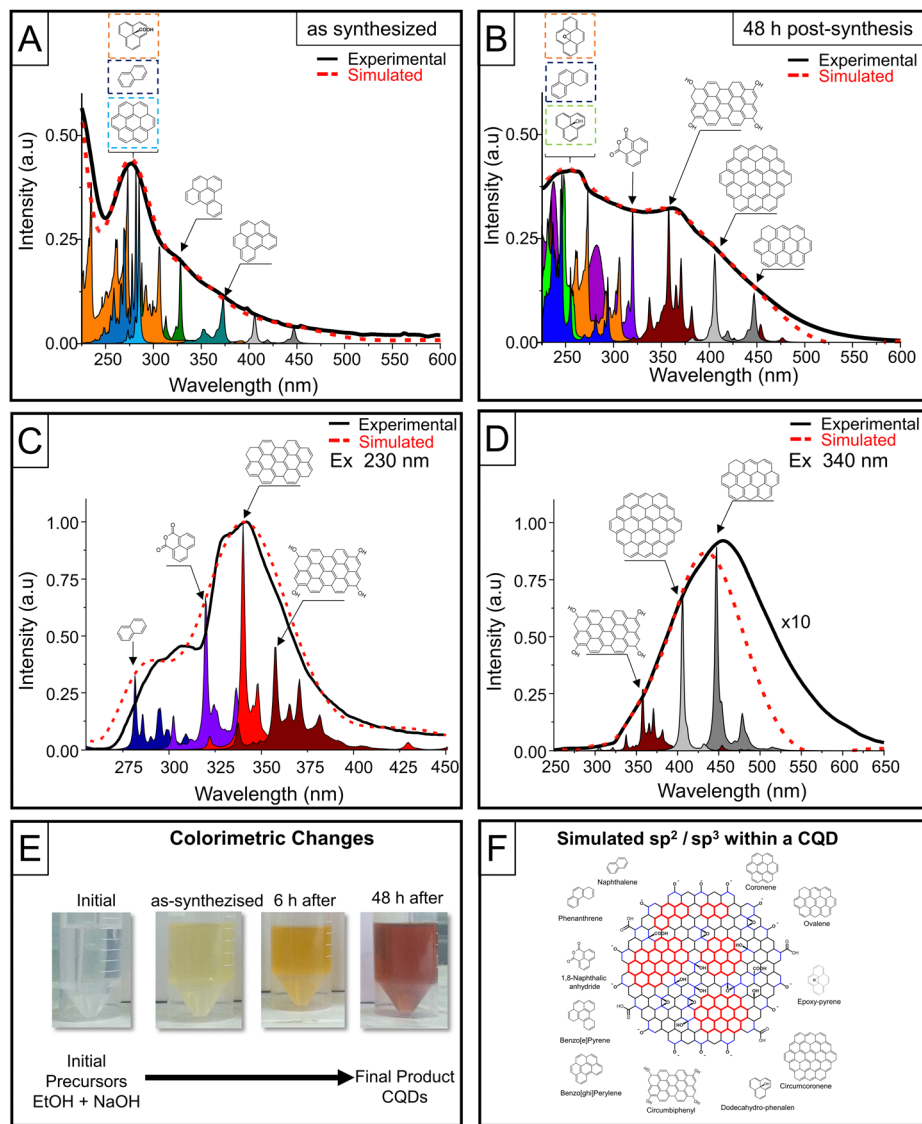


Fig. 3 Experimental and simulated UV-vis absorption for as-synthesized (A) and 48 h post-synthesis (B), averaged contribution of simulated PAHs is depicted in red. Emission spectra for CQDs measured at 230 nm (C) and 340 nm (D) excitation wavelength. Optical pictures showing colorimetric changes at different stages (E). A simulated CQD fully comprised of sp^2 aromatic rings (in red) and sp^3 (in blue) oxygen-containing groups within the basal plane and border (F).

observed at 285.7 eV and 1050 cm^{-1} , respectively. Finally, C–O–C groups were also confirmed for bands arising at 286.8 eV (C 1s) and 533.0 eV (O 1s) for XPS and at 1110 cm^{-1} for ATR-IR. Survey XPS spectra for CQDs shows atomic percentage C/O ratio of $\sim 80/20$ (Fig. S7, ESI[†]). Both techniques XPS and ATR-IR suggest a C=C sp^2 hybridized structure fully covered by sp^3 hybridized functional groups, indicating that CQDs are comprised of a collection of sp^2 domains embedded in a sp^3 framework.

Photodegradation of organic dyes

Fig. 5(A) shows successive representative UV-vis absorbance spectra for optimal concentrations of CQDs (0.8 mg mL^{-1}) dispersed in $1.0 \times 10^{-5}\text{ M}$ MB solution before and after 1, 2, 4, 5, 15, and 30 min exposure to UV-visible lamp (250–750 nm)

as indicated. The photodegradation of MB was monitored by looking at changes in intensity of two characteristic bands located at 663 and 613 nm corresponding to MB^+ and $(MB^+)_2$; respectively. It is expected that the kinetics of photodegradation for most organic dyes follows a pseudo-first order behavior, given by the influence of the initial concentration of the dye, irradiation conditions, nature of the photocatalyst, *etc.*⁶ Based on the Langmuir–Hinshelwood approximation adjusted for adsorption reactions at solid–liquid interfaces, we use the following equation:

$$\ln [C_{MB}/C_{MB}^0] = -k't \quad (1)$$

where; C_{MB} is the final concentration of MB after a period of time t under irradiation, C_{MB}^0 is the initial concentration of MB, k' corresponds to the apparent rate constant of the

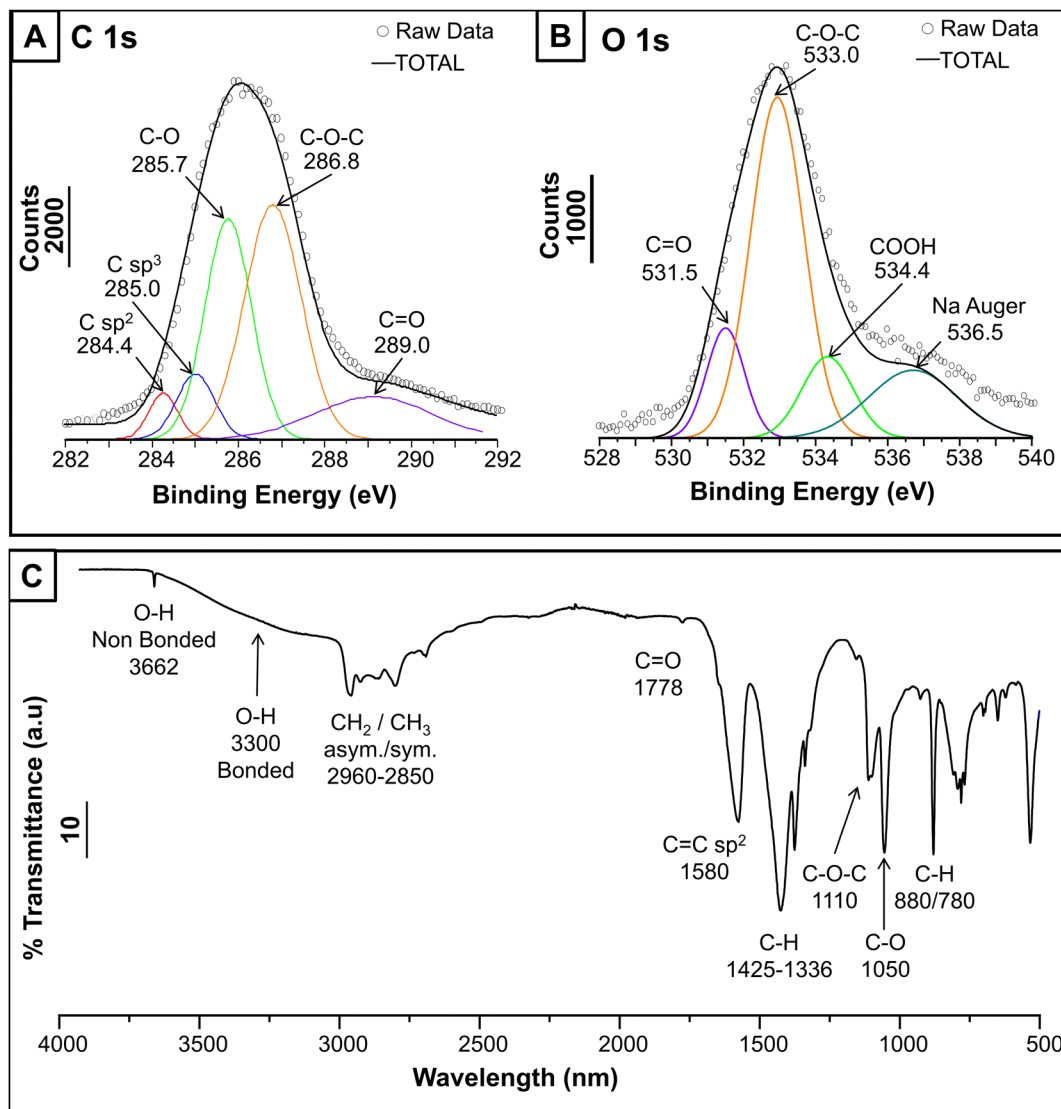


Fig. 4 Deconvoluted C 1s (A), O 1s (B) XPS spectra, and ATR-IR (C) bands for 48 h post-synthesis CQDs.

photocatalytic degradation (min^{-1}), and t corresponds to the time (in minutes) of irradiation. Fig. 5(B) shows the degradation of MB at three different starting concentrations (3.0×10^{-5} , 1.0×10^{-5} , and 4.7×10^{-6} M) later mixed with the same amount of CQDs (0.8 mg mL^{-1}). Fig. 5(C) confirms the pseudo-first order reaction as it shows a linear plot of natural log for $C_{\text{MB}}/C_{\text{MB}}^0$ ratio vs. the initial time under irradiation for up to 2 min of 4.7×10^{-6} M and 1.0×10^{-5} M MB solutions. The slopes for each curve determine the values of k' and the half life time, $t_{1/2}$, as indicated ($t_{1/2} = 0.693/k'$). Clearly, the photocatalytic activity given by the CQDs is practically equivalent for MB concentrations lower than 1.0×10^{-5} M.

Fig. 6(A) shows the photodegradation kinetics of 4.7×10^{-6} M MB tested at three different concentrations of CQDs as indicated. The general behavior is similar in all cases, with a degradation yield $> 85\%$ of the dye up to 30 min of irradiation. As expected, at higher CQDs concentrations, the initial rate reaches $\sim 97\%$ degradation within the first 10 min. This result

is quite remarkable from the point of view that most of the MB dye is photodegraded within just 5 to 10 min of UV-vis exposure. Fig. 6(B) compares a plot of C_t/C_0 vs. irradiation time for 3 samples: two control experiments with the optimal concentration of CQDs (0.8 mg mL^{-1}) performed with and without irradiation on a solution containing MB and irradiating only into a MB solution without photocatalyst. Without irradiation, there were no apparent changes whereas under irradiation the dye initially degraded very slowly (first 5 min) and ultimately reached $\sim 40\%$ after 30 min of exposure. When the optimal concentration of 0.8 mg mL^{-1} CQDs was mixed with MB, there was a sudden decrease in absorbance intensity down to $\sim 5\%$ of its initial value within the first 5 min under irradiation. This clearly indicates that CQDs alone are responsible for the fast and efficient photodegradation of the dye. Table S1 (ESI†) compares our work with Literature and highlights some important parameters including the type of carbon dots, type of organic dye, light source and power, and

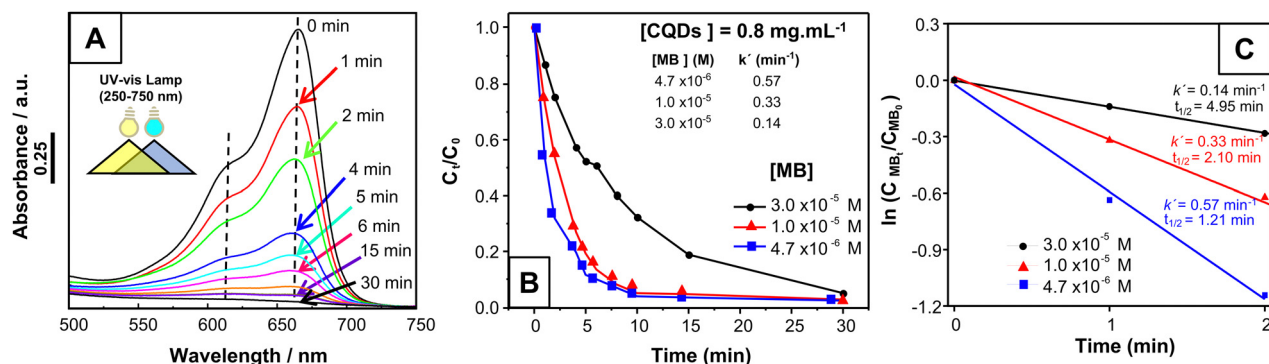


Fig. 5 Representative UV-vis absorbance spectra for optimal concentration of CQDs (0.8 mg mL⁻¹) dispersed in 1.0 × 10⁻⁵ M MB solution before (0 min) and after 1, 2, 4, 5, 6, 15, and 30 min exposure to 250–750 nm UV-visible lamp as indicated (A). 0.8 mg mL⁻¹ CQDs mixed with three different concentrations of MB (3.0 × 10⁻⁵, 1.0 × 10⁻⁵, and 4.7 × 10⁻⁶ M) to test the rate of degradation (B). Plot of natural log for C_{MB}/C_{MB,0} ratio vs. the initial time under irradiation for up to 2 min indicating linear curves for 4.7 × 10⁻⁶ M, 1.0 × 10⁻⁵ M, and 3.0 × 10⁻⁵ M MB solutions (C).

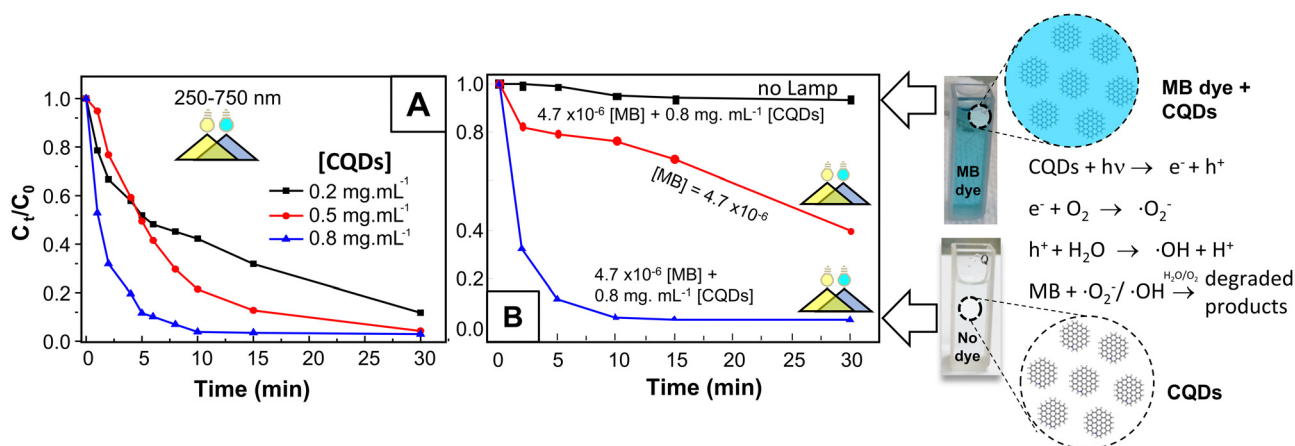


Fig. 6 Photodegradation of 4.7 × 10⁻⁶ M MB solution employing three different concentrations of CQDs (as indicated) (A). Plot of C_t/C₀ vs. irradiation time for two control experiments performed in dark and by irradiating on the MB solution as well as on the mixture of MB with CQDs at optimal concentrations as indicated (B). The panel next to B shows optical pictures of cuvettes before and after irradiation for 30 min along with the proposed mechanism of free radical generations. The cartoon represents the CQDs before and after the degradation of the dye.

degradation rate and time. A fair analysis would be to compare the performance of our CQDs with those irradiated with lamps of similar wavelength range. In this case, the as-synthesized CQDs outperform others regarding the kinetics of degradation being, in some cases, one order of magnitude faster than other catalysts exposed to similar conditions.^{43–46} It is reasonable to expect longer times of degradation when employing low energy lamps such as LED⁶ or visible lights^{6,43,47,48} due to the low power and longer irradiation wavelengths, respectively. Further studies will explore the irradiation of our catalyst with LED lights. Photodegradation of organic dyes using carbon dots has been an extensively researched area in past years demonstrating fast and steady generation of excitons upon illumination with UV-vis light.^{6,49} We believe that the oxygen-containing groups within the CQDs, confirmed by XPS and FT-IR techniques, play a crucial role in producing reactive oxygen radicals upon UV illumination, thus promoting photogenerated electrons from the LUMO to the HOMO band to ultimately transfer

electrons and dissolve oxygen in solution as indicated in the scheme next to Fig. 6(B).^{6,47}

Conclusions

In this study, we demonstrated a facile and efficient method for the electrosynthesis of graphene-like nanostructures *via* the oxidation of ethanol on the surface of Ni. In addition, we thoroughly characterized the product using various techniques including aberration corrected HR-TEM, AFM, XPS, UV-vis, Fluorescence, and FT-IR. The obtained product consists of highly crystalline carbon dots with a monodisperse size of approximately 3.0 nm and 2–3 graphene layers thick (0.7–1.0 nm). A considerable number of epoxy- and carbonyl-functional groups populate the as-synthesized CQDs, as indicated by XPS and FTIR measurements. Those functional groups are crucial because they produce an effective π truncation over the sp² character of the entire structure modifying their optical

response from a unique absorbance/emission peak to a sum of coexisting sp^2 subdomains present within each CQD. We performed TD-DFT using ORCA quantum chemistry package to calculate absorbance spectra and fluorescence emission of a list of possible candidates with <12 aromatic rings. Our simulations exhibited good agreement with the experimental data and provided a powerful platform to understand their optoelectronic properties. Furthermore, it is demonstrated the potential applications of these CQDs in photo-induced environmental remediation by testing their efficiency in degrading organic dyes. Upon 5 minutes of irradiation, CQDs were able to reduce by 95% the concentration of MB in aqueous solution. Notably, the as-synthesized CQDs exhibited superior kinetics of degradation compared to other catalysts under similar conditions, in some cases, showing one order of magnitude faster degradation. Our study highlights the potential of CQDs for the development of novel organic electronics and their use in environmental remediation applications.

Author contributions

The manuscript was collaboratively created with contributions from all authors, who have provided their approval for the final version of the manuscript.

Conflicts of interest

There are no conflicts to declare.

Acknowledgements

We gratefully acknowledge financial support from PICT (2019–2188) and Proyecto de Incentivos 2019-X-887 from UNLP. SB and FF acknowledge CONICET for their doctoral scholarships. We also acknowledge the financial support of European Commission through Marie Skłodowska-Curie Actions H2020 RISE with the projects MELON (grant no. 872631) and ULTIMATE-I (grant no. 101007825). Authors would like to acknowledge the access of equipment of “Servicio General de Apoyo a la Investigación (SAI), Universidad de Zaragoza” and LAMARX-SNM at Universidad Nacional de Córdoba (UNC), Argentina.

Notes and references

- Z. Fan, S. Zhou, C. Garcia, L. Fan and J. Zhou, PH-Responsive Fluorescent Graphene Quantum Dots for Fluorescence-Guided Cancer Surgery and Diagnosis, *Nanoscale*, 2017, 9(15), 4928–4933, DOI: [10.1039/C7NR00888K](https://doi.org/10.1039/C7NR00888K).
- M. Llaver, S. D. Barrionuevo, E. Prieto, R. G. Wuilloud and F. J. Ibañez, Functionalized Graphene Quantum Dots Obtained from Graphene Foams Used for Highly Selective Detection of Hg^{2+} in Real Samples, *Anal. Chim. Acta*, 2022, 1232, 340422, DOI: [10.1016/j.aca.2022.340422](https://doi.org/10.1016/j.aca.2022.340422).
- M. Llaver, S. D. Barrionuevo, H. Troiani, R. G. Wuilloud and F. J. Ibañez, Highly Selective and Sensitive Fluorescent Determination of Fe^{3+} within Alcoholic Beverages with 1,5-Diphenylcarbazone-Functionalized Graphene Quantum Dots, *Talanta Open*, 2023, 7, 100202, DOI: [10.1016/j.talo.2023.100202](https://doi.org/10.1016/j.talo.2023.100202).
- M. M. Messina, S. D. Barrionuevo, M. E. Coustet, M. P. Kreuzer, F. D. Saccone, P. C. dos Santos Claro and F. J. Ibañez, Graphene and Carbon Dots for Photoanodes with Enhanced Performance, *ACS Appl. Nano Mater.*, 2021, 4(7), 7309–7318, DOI: [10.1021/acsnano.1c01295](https://doi.org/10.1021/acsnano.1c01295).
- Y. Yan, J. Chen, N. Li, J. Tian, K. Li, J. Jiang, J. Liu, Q. Tian and P. Chen, Systematic Bandgap Engineering of Graphene Quantum Dots and Applications for Photocatalytic Water Splitting and CO_2 Reduction, *ACS Nano*, 2018, 12(4), 3523–3532, DOI: [10.1021/acsnano.8b00498](https://doi.org/10.1021/acsnano.8b00498).
- S. Umrao, P. Sharma, A. Bansal, R. Sinha, R. K. Singh and A. Srivastava, Multi-Layered Graphene Quantum Dots Derived Photodegradation Mechanism of Methylene Blue, *RSC Adv.*, 2015, 5(64), 51790–51798, DOI: [10.1039/c5ra07310c](https://doi.org/10.1039/c5ra07310c).
- W. Chen, G. Lv, W. Hu, D. Li, S. Chen and Z. Dai, Synthesis and Applications of Graphene Quantum Dots: A Review, *Nanotechnol. Rev.*, 2018, 7(2), 157–185, DOI: [10.1515/ntrev-2017-0199](https://doi.org/10.1515/ntrev-2017-0199).
- L. Cui, X. Ren, M. Sun, H. Liu and L. Xia, Carbon Dots: Synthesis, Properties and Applications, *Nanomaterials*, 2021, 11(12), 3419, DOI: [10.3390/nano11123419](https://doi.org/10.3390/nano11123419).
- D. Rocco, V. G. Moldoveanu, M. Feroci, M. Bortolami and F. Vetica, Electrochemical Synthesis of Carbon Quantum Dots, *ChemElectroChem*, 2023, e202201104, DOI: [10.1002/celec.202201104](https://doi.org/10.1002/celec.202201104).
- J. Deng, Q. Lu, N. Mi, H. Li, M. Liu, M. Xu, L. Tan, Q. Xie, Y. Zhang and S. Yao, Electrochemical Synthesis of Carbon Nanodots Directly from Alcohols, *Chem. – Eur. J.*, 2014, 20(17), 4993–4999, DOI: [10.1002/chem.201304869](https://doi.org/10.1002/chem.201304869).
- Y. Hou, Q. Lu, J. Deng, H. Li and Y. Zhang, One-Pot Electrochemical Synthesis of Functionalized Fluorescent Carbon Dots and Their Selective Sensing for Mercury Ion, *Anal. Chim. Acta*, 2015, 866, 69–74, DOI: [10.1016/j.aca.2015.01.039](https://doi.org/10.1016/j.aca.2015.01.039).
- F. Niu, Y. Xu, M. Liu, J. Sun, P. Guo and J. Liu, Bottom-up Electrochemical Preparation of Solid-State Carbon Nanodots Directly from Nitriles/Ionic Liquids Using Carbon-Free Electrodes and the Applications in Specific Ferric Ion Detection and Cell Imaging, *Nanoscale*, 2016, 8(10), 5470–5477, DOI: [10.1039/C6NR00023A](https://doi.org/10.1039/C6NR00023A).
- Y.-S. Lee, C.-C. Hu and T.-C. Chiu, Electrochemical Synthesis of Fluorescent Carbon Dots for the Selective Detection of Chlortetracycline, *J. Environ. Chem. Eng.*, 2022, 10(3), 107413, DOI: [10.1016/j.jece.2022.107413](https://doi.org/10.1016/j.jece.2022.107413).
- L. Hu, H. Li, C. Liu, Y. Song, M. Zhang, H. Huang, Y. Liu and Z. Kang, Chiral Evolution of Carbon Dots and the Tuning of Laccase Activity, *Nanoscale*, 2018, 10(5), 2333–2340, DOI: [10.1039/C7NR08335A](https://doi.org/10.1039/C7NR08335A).
- D. Pan, J. Zhang, Z. Li and M. Wu, Hydrothermal Route for Cutting Graphene Sheets into Blue-Luminescent Graphene Quantum Dots, *Adv. Mater.*, 2010, 22(6), 734–738, DOI: [10.1002/adma.200902825](https://doi.org/10.1002/adma.200902825).

- 16 Z. Liu, F. Li, Y. Luo, M. Li, G. Hu, X. Pu, T. Tang, J. Wen, X. Li and W. Li, Size Effect of Graphene Quantum Dots on Photoluminescence, *Molecules*, 2021, **26**(13), 3922, DOI: [10.3390/molecules26133922](https://doi.org/10.3390/molecules26133922).
- 17 A. Rakovich and T. Rakovich, Semiconductor versus Graphene Quantum Dots as Fluorescent Probes for Cancer Diagnosis and Therapy Applications, *J. Mater. Chem. B*, 2018, **6**(18), 2690–2712, DOI: [10.1039/C8TB00153G](https://doi.org/10.1039/C8TB00153G).
- 18 S. Wang, Y. Dong, C. He, Y. Gao, N. Jia, Z. Chen and W. Song, The Role of Sp²/Sp³ Hybrid Carbon Regulation in the Nonlinear Optical Properties of Graphene Oxide Materials, *RSC Adv.*, 2017, **7**(84), 53643–53652, DOI: [10.1039/C7RA10505C](https://doi.org/10.1039/C7RA10505C).
- 19 S. Lai, Y. Jin, L. Shi, R. Zhou, Y. Zhou and D. An, Mechanisms behind Excitation- and Concentration-Dependent Multicolor Photoluminescence in Graphene Quantum Dots, *Nanoscale*, 2020, **12**(2), 591–601, DOI: [10.1039/C9NR08461D](https://doi.org/10.1039/C9NR08461D).
- 20 S. Kim, S. W. Hwang, M.-K. Kim, D. Y. Shin, D. H. Shin, C. O. Kim, S. B. Yang, J. H. Park, E. Hwang, S.-H. Choi, G. Ko, S. Sim, C. Sone, H. J. Choi, S. Bae and B. H. Hong, Anomalous Behaviors of Visible Luminescence from Graphene Quantum Dots: Interplay between Size and Shape, *ACS Nano*, 2012, **6**(9), 8203–8208, DOI: [10.1021/nn302878r](https://doi.org/10.1021/nn302878r).
- 21 N. V. Tepliakov, E. V. Kundeleev, P. D. Khavlyuk, Y. Xiong, M. Yu Leonov, W. Zhu, A. V. Baranov, A. V. Fedorov, A. L. Rogach and I. D. Rukhlenko, Sp²–Sp³-Hybridized Atomic Domains Determine Optical Features of Carbon Dots, *ACS Nano*, 2019, **13**(9), 10737–10744, DOI: [10.1021/acsnano.9b05444](https://doi.org/10.1021/acsnano.9b05444).
- 22 X. Mercier, O. Carrivain, C. Irimiea, A. Faccinetto and E. Therssen, Dimers of Polycyclic Aromatic Hydrocarbons: The Missing Pieces in the Soot Formation Process, *Phys. Chem. Chem. Phys.*, 2019, **21**(16), 8282–8294, DOI: [10.1039/C9CP00394K](https://doi.org/10.1039/C9CP00394K).
- 23 L. F. Melia, S. D. Barrionuevo and F. J. Ibañez, Think Outside the Lab: Modeling Graphene Quantum Dots in Pandemic Times, *J. Chem. Educ.*, 2022, **99**(2), 745–751, DOI: [10.1021/acs.jchemed.1c00879](https://doi.org/10.1021/acs.jchemed.1c00879).
- 24 H. Yoon, Y. H. Chang, S. H. Song, E.-S. Lee, S. H. Jin, C. Park, J. Lee, B. H. Kim, H. J. Kang, Y.-H. Kim and S. Jeon, Intrinsic Photoluminescence Emission from Sub-domained Graphene Quantum Dots, *Adv. Mater.*, 2016, **28**(26), 5255–5261, DOI: [10.1002/adma.201600616](https://doi.org/10.1002/adma.201600616).
- 25 M. Fu, F. Ehrat, Y. Wang, K. Z. Milowska, C. Reckmeier, A. L. Rogach, J. K. Stolarczyk, A. S. Urban and J. Feldmann, Carbon Dots: A Unique Fluorescent Cocktail of Polycyclic Aromatic Hydrocarbons, *Nano Lett.*, 2015, **15**(9), 6030–6035, DOI: [10.1021/acs.nanolett.5b02215](https://doi.org/10.1021/acs.nanolett.5b02215).
- 26 L. Wang, Y. Wang, T. Xu, H. Liao, C. Yao, Y. Liu, Z. Li, Z. Chen, D. Pan, L. Sun and M. Wu, Gram-Scale Synthesis of Single-Crystalline Graphene Quantum Dots with Superior Optical Properties, *Nat. Commun.*, 2014, **5**(1), 5357, DOI: [10.1038/ncomms6357](https://doi.org/10.1038/ncomms6357).
- 27 S. Chen, N. Ullah, T. Wang and R.-Q. Zhang, Tuning Optical Properties of Graphene Quantum Dots by Selective Oxidation: A Theoretical Perspective, *J. Mater. Chem. C*, 2018, **6**, DOI: [10.1039/C8TC02083C](https://doi.org/10.1039/C8TC02083C).
- 28 M. A. Sk, A. Ananthanarayanan, L. Huang, K. H. Lim and P. Chen, Revealing the Tunable Photoluminescence Properties of Graphene Quantum Dots, *J. Mater. Chem. C*, 2014, **2**(34), 6954–6960, DOI: [10.1039/C4TC01191K](https://doi.org/10.1039/C4TC01191K).
- 29 B. Shi, D. Nachtigallová, A. J. A. Aquino, F. B. C. Machado and H. Lischka, High-Level Theoretical Benchmark Investigations of the UV-Vis Absorption Spectra of Paradigmatic Polycyclic Aromatic Hydrocarbons as Models for Graphene Quantum Dots, *J. Chem. Phys.*, 2019, **150**(12), 124302, DOI: [10.1063/1.5086760](https://doi.org/10.1063/1.5086760).
- 30 F. Neese, F. Wennmohs, U. Becker and C. Riplinger, The ORCA Quantum Chemistry Program Package, *J. Chem. Phys.*, 2020, **152**(22), 224108, DOI: [10.1063/5.0004608](https://doi.org/10.1063/5.0004608).
- 31 T. Petrenko and F. Neese, Analysis and Prediction of Absorption Band Shapes, Fluorescence Band Shapes, Resonance Raman Intensities, and Excitation Profiles Using the Time-Dependent Theory of Electronic Spectroscopy, *J. Chem. Phys.*, 2007, **127**(16), 164319, DOI: [10.1063/1.2770706](https://doi.org/10.1063/1.2770706).
- 32 Y. Shen, S. Su, W. Zhao, S. Cheng, T. Xu, K. Yin, L. Chen, L. He, Y. Zhou, H. Bi, S. Wan, Q. Zhang, L. Wang, Z. Ni, F. Banhart, G. A. Botton, F. Ding, R. S. Ruoff and L. Sun, Sub-4 Nm Nanodiamonds from Graphene-Oxide and Nitrated Polycyclic Aromatic Hydrocarbons at 423 K, *ACS Nano*, 2021, **15**(11), 17392–17400, DOI: [10.1021/acsnano.1c00209](https://doi.org/10.1021/acsnano.1c00209).
- 33 M. Liu, Y. Xu, F. Niu, J. J. Gooding and J. Liu, Carbon Quantum Dots Directly Generated from Electrochemical Oxidation of Graphite Electrodes in Alkaline Alcohols and the Applications for Specific Ferric Ion Detection and Cell Imaging, *Analyst*, 2016, **141**(9), 2657–2664, DOI: [10.1039/C5AN02231B](https://doi.org/10.1039/C5AN02231B).
- 34 R. Qiang, W. Sun, K. Hou, Z. Li, J. Zhang, Y. Ding, J. Wang and S. Yang, Electrochemical Trimming of Graphene Oxide Affords Graphene Quantum Dots for Fe³⁺ Detection, *ACS Appl. Nano Mater.*, 2021, **4**(5), 5220–5229, DOI: [10.1021/acsanm.1c00621](https://doi.org/10.1021/acsanm.1c00621).
- 35 G. Rajender and P. K. Giri, Formation Mechanism of Graphene Quantum Dots and Their Edge State Conversion Probed by Photoluminescence and Raman Spectroscopy, *J. Mater. Chem. C*, 2016, **4**(46), 10852–10865, DOI: [10.1039/C6TC03469A](https://doi.org/10.1039/C6TC03469A).
- 36 J. W. Patterson, The Ultraviolet Absorption Spectra of Coronene, *J. Am. Chem. Soc.*, 1942, **64**(6), 1485–1486, DOI: [10.1021/ja01258a505](https://doi.org/10.1021/ja01258a505).
- 37 J. Fetzer, The Chemistry and Analysis of Large PAHs, *Polycyclic Aromat. Compd.*, 2007, **27**, 143–162, DOI: [10.1080/10406630701268255](https://doi.org/10.1080/10406630701268255).
- 38 R. Waris, M. A. Rembert, D. M. Sellers, W. E. Acree, K. W. Street and J. C. Fetzer, Polycyclic Aromatic Hydrocarbon Solute Probes. Part II. Effect of Solvent Polarity on the Fluorescence Emission Fine Structures of Coronene Derivatives, *Analyst*, 1989, **114**(2), 195–199, DOI: [10.1039/AN9891400195](https://doi.org/10.1039/AN9891400195).
- 39 T. Kou, M. Chen, F. Wu, T. J. Smart, S. Wang, Y. Wu, Y. Zhang, S. Li, S. Lall, Z. Zhang, Y.-S. Liu, J. Guo, G. Wang, Y. Ping and Y. Li, Carbon Doping Switching on

- the Hydrogen Adsorption Activity of NiO for Hydrogen Evolution Reaction, *Nat. Commun.*, 2020, **11**(1), 590, DOI: [10.1038/s41467-020-14462-2](https://doi.org/10.1038/s41467-020-14462-2).
- 40 Thermo Scientific Avantage Data System for XPS. <https://www.thermofisher.com/ar/es/home/materials-science/learning-center/periodic-table.html>.
- 41 C. Powell, X-Ray Photoelectron Spectroscopy Database XPS, Version 4.1, NIST Standard Reference Database 20, 1989, DOI: [10.18434/T4T88K](https://doi.org/10.18434/T4T88K).
- 42 J. Coates, Interpretation of Infrared Spectra, A Practical Approach, *Encyclopedia of Analytical Chemistry*, John Wiley & Sons, Ltd, 2006, DOI: [10.1002/9780470027318.a5606](https://doi.org/10.1002/9780470027318.a5606).
- 43 L. Cheng and X. Dong, Carbonaceous 0D/2D Composite Photocatalyst for Degradation of Organic Dyes, *Diamond Relat. Mater.*, 2020, **109**, 108096, DOI: [10.1016/j.diamond.2020.108096](https://doi.org/10.1016/j.diamond.2020.108096).
- 44 H. Safardoust-Hojaghan and M. Salavati-Niasari, Degradation of Methylene Blue as a Pollutant with N-Doped Graphene Quantum Dot/Titanium Dioxide Nanocomposite, *J. Cleaner Prod.*, 2017, **148**, 31–36, DOI: [10.1016/j.jclepro.2017.01.169](https://doi.org/10.1016/j.jclepro.2017.01.169).
- 45 B. Ahmed, S. Kumar, A. K. Ojha, F. Hirsch, S. Riese and I. Fischer, Facile Synthesis and Photophysics of Graphene Quantum Dots, *J. Photochem. Photobiol., A*, 2018, **364**, 671–678, DOI: [10.1016/j.jphotochem.2018.07.006](https://doi.org/10.1016/j.jphotochem.2018.07.006).
- 46 A. Ibarbia, H. J. Grande and V. Ruiz, On the Factors behind the Photocatalytic Activity of Graphene Quantum Dots for Organic Dye Degradation, *Part. Part. Syst. Charact.*, 2020, **37**(5), 2000061, DOI: [10.1002/ppsc.202000061](https://doi.org/10.1002/ppsc.202000061).
- 47 K. Akbar, E. Moretti and A. Vomiero, Carbon Dots for Photocatalytic Degradation of Aqueous Pollutants: Recent Advancements, *Adv. Opt. Mater.*, 2021, **9**(17), 2100532, DOI: [10.1002/adom.202100532](https://doi.org/10.1002/adom.202100532).
- 48 Z. Niazi, E. K. Goharshadi, M. Mashreghi and M. N. Jorabchi, Highly Efficient Solar Photocatalytic Degradation of a Textile Dye by TiO₂/Graphene Quantum Dots Nanocomposite, *Photochem. Photobiol. Sci.*, 2021, **20**(1), 87–99, DOI: [10.1007/s43630-020-00005-7](https://doi.org/10.1007/s43630-020-00005-7).
- 49 Y. Zhou, E. M. Zahran, B. A. Quiroga, J. Perez, K. J. Mintz, Z. Peng, P. Y. Liyanage, R. R. Pandey, C. C. Chusuei and R. M. Leblanc, Size-Dependent Photocatalytic Activity of Carbon Dots with Surface-State Determined Photoluminescence, *Appl. Catal., B*, 2019, **248**, 157–166, DOI: [10.1016/j.apcatb.2019.02.019](https://doi.org/10.1016/j.apcatb.2019.02.019).